



ELSEVIER

Contents lists available at ScienceDirect

Deep-Sea Research II

journal homepage: www.elsevier.com/locate/dsr2

Glider observations of the Dotson Ice Shelf outflow

Travis Miles^{a,*}, Sang Hoon Lee^b, Anna Wählin^c, Ho Kyung Ha^{b,d}, Tae Wan Kim^b, Karen M. Assmann^c, Oscar Schofield^a^a Department of Marine and Coastal Sciences, Rutgers University, New Brunswick, NJ 08901, USA^b Korea Polar Research Institute, Incheon 406-840, South Korea^c Department of Marine Sciences, University of Gothenburg, Gothenburg, Sweden^d Department of Ocean Sciences, Inha University, Incheon 402-751, South Korea

ARTICLE INFO

Available online 6 September 2015

Keywords:

Glanders
Circumpolar Deep Water
Dotson Ice Shelf
Amundsen Sea

ABSTRACT

The Amundsen Sea is one of the most productive polynyas in the Antarctic per unit area and is undergoing rapid changes including a reduction in sea ice duration, thinning ice sheets, retreat of glaciers and the potential collapse of the Thwaites Glacier in Pine Island Bay. A growing body of research has indicated that these changes are altering the water mass properties and associated biogeochemistry within the polynya. Unfortunately difficulties in accessing the remote location have greatly limited the amount of *in situ* data that has been collected. In this study data from a Teledyne-Webb Slocum glider was used to supplement ship-based sampling along the Dotson Ice Shelf (DIS). This autonomous underwater vehicle revealed a detailed view of a meltwater laden outflow from below the western flank of the DIS. Circumpolar Deep Water intruding onto the shelf drives glacial melt and the supply of macronutrients that, along with ample light, supports the large phytoplankton blooms in the Amundsen Sea Polynya. Less well understood is the source of micronutrients, such as iron, necessary to support this bloom to the central polynya where chlorophyll concentrations are highest. This outflow region showed decreasing optical backscatter with proximity to the bed indicating that particulate matter was sourced from the overlying glacier rather than resuspended sediment. This result suggests that particulate iron, and potentially phytoplankton primary productivity, is intrinsically linked to the magnitude and duration of sub-glacial melt from Circumpolar Deep Water intrusions onto the shelf.

© 2015 The Authors. Published by Elsevier Ltd. This is an open access article under the CC BY-NC-ND license (<http://creativecommons.org/licenses/by-nc-nd/4.0/>).

1. Introduction

The collapse of the West Antarctic ice sheet appears to be irreversible (Joughin et al., 2014a; Mouginot et al., 2014; Rignot et al., 2014) due to changing winds, ocean warming, and changes in ocean circulation (Jenkins et al., 2010; Pritchard et al., 2012; Schmidtke et al., 2014). The largest changes are expressed in the Amundsen Sea, in the Southeast Pacific sector of the Antarctic. Climate changes in the Amundsen Sea, and its associated glaciers, include reductions in sea ice duration by 60 ± 9 days (Stammerjohn et al., 2012), thinning ice sheets (Rignot et al., 2014), and retreating glaciers (Rignot and Jacobs, 2002; Rignot et al., 2008, 2014). Recent studies (Joughin et al., 2014b; Sutterley et al., 2014) have indicated that the Thwaites Glacier in Pine Island Bay is losing mass at a rate of 83 ± 5 Gt yr⁻¹ and has begun to undergo early-stage collapse, with the potential for causing over 1 mm yr⁻¹ of global sea level rise.

These changes are altering the water mass properties and associated biogeochemistry in the polynya. Unfortunately, difficulties in accessing the remote location have greatly limited the amount of *in situ* data that has been collected, which limits our understanding of the physical mechanisms that regulate the biological processes in this area (Lee et al., 2012).

The Amundsen Sea Polynya (ASP) has one of the highest satellite derived mean phytoplankton concentrations in the Antarctic with seasonally averaged chlorophyll concentrations (2.18 ± 3.01 mg m⁻³) larger than the more frequently studied Ross Sea Polynya (1.51 ± 1.52 mg m⁻³) (Arrigo and van Dijken, 2003). With high levels of unused macronutrients year-round, the availability of iron (Fe) or light, or both, is thought to limit primary productivity in the coastal Antarctic (Sunda and Huntsman, 1997; Boyd, 2002; Arrigo et al., 2012). Strong relationships exist between phytoplankton and the depth of the upper mixed layer suggesting the importance of light (Schofield et al., *in press*) while deck board incubations also confirm the importance of Fe (Alderkamp et al., 2015). Previous studies have observed high levels of dissolved (Alderkamp et al., 2012; Arrigo et al., 2012; Gerringa et al., 2012) and particulate (Planquette et al., 2013) Fe in proximity to the Pine Island Ice Shelf (PIIS) and the Crosson, Dotson, and Getz ice shelves

* Correspondence to: Department of Marine and Coastal Sciences, Rutgers University, Center for Ocean Observing Leadership, 71 Dudley Rd. New Brunswick, NJ. Tel.: 848 932 3293.

E-mail address: tnmiles@marine.rutgers.edu (T. Miles).

to the west. Likely sources of this Fe include basal melt from beneath ice shelves (Gerringa et al., 2012; Yager et al., 2012), and direct observations have been made of dissolved and particulate Fe in the meltwater-laden outflow from beneath the Dotson Ice Shelf (DIS) (Alderkamp et al., 2015).

The main driver of basal melt is believed to be the warm Circumpolar Deep Water (CDW) (up to 4 °C above the freezing point) intruding onto the Amundsen Sea continental shelf and below ice shelves (Jenkins et al., 2010; Jacobs et al., 2011; Dutrieux et al., 2014). Processes controlling the flow of warm CDW on the shelf are only broadly identified and there is a lack of sufficiently long (decadal or more) time series to enable linking of the oceanographic processes to climate variability. These processes include the establishment of an eastward undercurrent (Chavanne et al., 2010; Walker et al., 2013); bottom Ekman transport (Wählin et al., 2012); eddies (Thompson et al., 2014) and wind (Thoma et al., 2008). The cross shelf-break inflow to the DIS occurs through the same outer trough that channels CDW toward the Getz Ice Shelf, also known as the Dotson Trough. Closer to the ice shelves the trough branches out into three deep basins, leading into the sub-ice cavities below the Dotson and Getz ice shelves (Fig. 1). Observations of the circulation in these troughs (Walker et al., 2007; Wählin et al., 2010) show that CDW inflows are located on their eastern flanks and mooring data indicate the circulation patterns are persistent and steady (Arneborg et al., 2012; Assmann et al., 2013; Wählin et al., 2013). The outflows on their western flanks are colder and fresher due to the addition of meltwater (Ha et al., 2014; Wählin et al., 2015). As these water masses reach the glaciers and ice shelves the warm CDW melts ice and forms a modified CDW (mCDW) and meltwater mixture (Jenkins, 1999; Jenkins and Jacobs, 2008; Jenkins et al., 2010; Wählin et al., 2010; Jacobs et al., 2011; Randall-Goodwin et al., 2015). Few observations of the ocean circulation and water properties at ice shelf fronts exist. The paucity of data in this region is largely due to the remote location of the Amundsen Sea as well as limited resources to investigate the ~1200 km of coastline. A summary of three US-led cruises to the ice shelf fronts in the Amundsen Sea Embankment (ASE) can be found in Jacobs et al. (2013). A large number of these transects show a core of CDW leaning on the eastern flank of the entrance to the ice shelf cavity, i.e. associated with geostrophic flow into the cavity, and cooler, fresher, and more buoyant, water is commonly found on the western side higher up in the water column, associated with a geostrophic flow out of the cavity. Focused field campaigns (Jacobs et al., 1996, 2011) have observed this phenomenon along the Pine Island Glacier in 1994 and 2009.

The first observation of an outflow of meltwater-laden mCDW in the central Amundsen shelf area was done in 4 moorings placed in the Dotson Trough (Ha et al., 2014), where a steady outflow on the eastern flank of Dotson Trough was observed throughout 2011. Similar hydrographic properties at a nearby location were also recorded during 2012–2013 (Wählin et al., 2015). Due to challenging ice conditions cross-trough CTD transects extending sufficiently far west to cover the entire outflow do not exist. The estimates of volume flux derived from the single-point moorings are hence uncertain. Based on the most complete CTD transect, an outflow corresponding to about 1/3 of the inflow was obtained (Ha et al., 2014). It is not known which path the remainder of the outflow takes. Explanations that have been proposed include flow in a narrow coastal current; below a possible tunnel underneath the Getz Ice Shelf; or into the surface mixed layer (Ha et al., 2014). More recent work shows a similar circulation pattern, with outflow along the far western edge of the DIS with high meltwater concentrations (Randall-Goodwin et al., 2015). In this work we present observations from the front of the DIS collected by ship and a Teledyne-Webb Slocum glider. The glider permitted high vertical and horizontal resolution sampling in a relatively short time frame (days). The physical and bio-optical datasets collected provide a detailed snapshot of the location and water properties of the DIS outflow with optical backscatter profiles indicating ice melt as the primary source of particulate matter from the sub-glacial cavity to the near-surface ASP.

2. Methods

Data was collected in the Amundsen Sea during January of 2014 as part of the Korea Polar Research Institute (KOPRI) ANA04B cruise onboard the IBRV *Araon*. This cruise was designed with the goal of understanding regional circulation and how that circulation may impact the biogeochemistry of the ASP. A total of 35 hydrographic stations were sampled and two Teledyne-Webb Slocum gliders (one shallow class (< 100 m) and one deep class (< 1000 m)) were deployed and recovered during ANA04B. As this paper is focused on the transport of mCDW, only the glider capable of profiling to 1000 m was able to provide relevant data and was used in this paper.

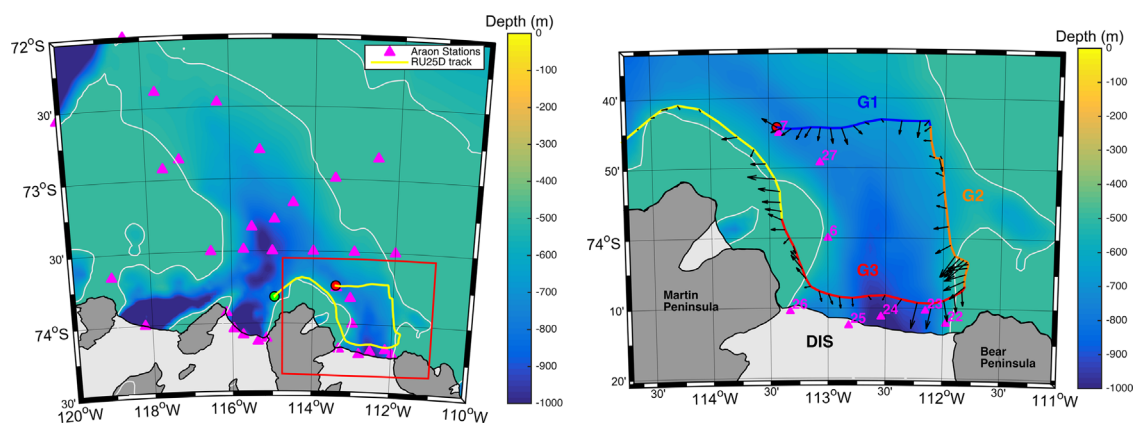


Fig. 1. (Left panel) Map of the KOPRI cruise ANA04B study area in the Amundsen Sea with hydrographic stations sampled by the IBRV *Araon* (magenta triangles) and the track of the glider RU25D (yellow line) with the deployment location (red circle) and the recovery location (green circle). The red box bounds the displayed area in the right panel. (Right panel) zoomed in view of the glider and ship sampling area directly in front of the Dotson Ice Shelf with the glider track separated into three distinct tracks including across trough (blue G1), along the eastern flank (orange G2), and along the Dotson Ice Shelf Face (red G3). Ship sampling locations are numbered and continue to be represented by magenta triangles. There are additional ship-based stations that were collected off the continental shelf not included in this map. Black vectors represent the depth- and time- averaged glider velocities.

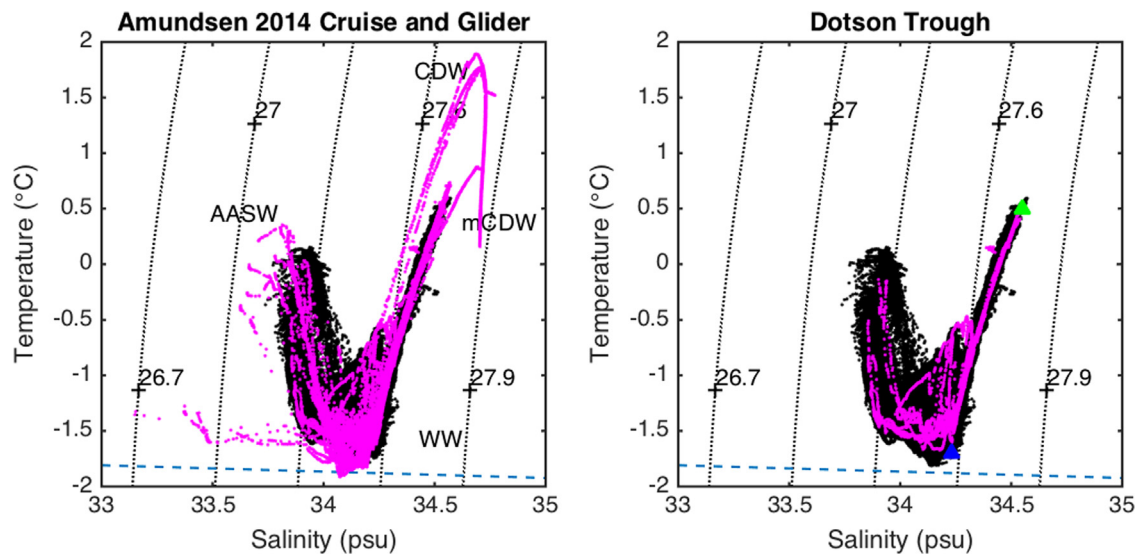


Fig. 2. (Left panel) A temperature and salinity diagram of all data collected by the IBRV Araon (magenta) and glider RU25D (black), with labels of the major water masses. (Right panel) A subset of the data collected directly in front of the Dotson Ice Shelf, corresponding to locations shown in the right panel of Fig. 1. Green and blue triangles represent the mCDW and WW end-members used for calculating meltwater fractions.

2.1. Ship sampling

Ship-based measurements were made from a rosette that included Niskin bottles for discrete water sampling, a Seabird SBE-911plus with dual conductivity temperature and depth (CTD) sensors, and velocity structure from a 300-kHz Teledyne-RDI lowered acoustic Doppler current profiler (LADCP). During upcast of the CTD, discrete water samples were collected and used to calibrate the temperature and conductivity probes following standard practices. The LADCP data was processed using Lamont Doherty Earth Observatory (LDEO) Matlab[®]-based software version IX (Thurnherr, 2010). Tidal signals were removed from the LADCP-measured velocity profiles using a 10-component barotropic tide model, CATS2008b (Padman et al., 2002).

2.2. Glider sampling

Teledyne-Webb Slocum gliders are buoyancy driven mobile sensor platforms with interchangeable and customizable science bays (Webb et al., 2001; Davis et al., 2003; Schofield et al., 2007). These 1.5 m torpedo shaped autonomous underwater vehicles profile the water column in a sawtooth pattern by shifting small amounts of ballast to dive and climb at $\sim 15\text{--}20\text{ cm s}^{-1}$. Wings, vehicle shape, and the set nominal pitch angle of $\sim 26^\circ$ result in horizontal speeds of $\sim 20\text{--}30\text{ cm s}^{-1}$, or $\sim 20\text{ km per day}$ depending on ambient current conditions. Vehicle navigation is done using “dead-reckoning” to a set waypoint. When the glider surfaces an air-bladder in the aft section inflates, raising the tail section out of the water. An iridium satellite phone antenna within the tail section transmits data to shore and receives new mission characteristics depending on the sampling strategies designed by the operator. Oceanographic data is collected at two-second intervals resulting in high vertical resolutions. Gliders have been used in numerous difficult to sample environments including on continental shelves (Castelao et al., 2010; Adams et al., 2013; Pelland et al., 2013), long duration cross-basin missions (Glenn et al., 2011), within storms (Glenn et al., 2008; Miles et al., 2013; Mrvaljevic et al., 2013), and have had a significant presence in the Western Antarctic (Kahl et al., 2010; Schofield et al., 2013; Kohut et al., 2015).

The glider used in this study was a Deep glider (RU25D) rated to 1000 meters, near the maximum depth of the approach to the Dotson Trough. The glider was deployed on January 4th, 2014 at 113.4°W (Fig. 1) and 73.74°S and performed three distinct sections, with the first over 40 km west to east across the Dotson Trough at 74°S , the second was 46 km southward toward the DIS on the eastern flank of the Dotson Trough. The third transect was 54 km across the face of the DIS from east to west and was approximately 5 km from the ice edge and continued westward around the Martin Peninsula and toward the Getz Ice Shelf until recovery on January 13th. Throughout this deployment RU25D collected a total of 206 profiles and traveled 234 km in 9 days.

RU25D was equipped with a suite of oceanographic sensors including an un-pumped Seabird glider payload CTD (GPCTD), an Aanderaa Oxygen Optode (Model 3835), and a Wetlabs Environmental Characterization Optics puck (ECO-triplet). Glider temperature and conductivity measurements were compared with shipboard CTD casts on deployment and recovery to ensure data quality, as well as with a calibrated laboratory CTD prior to deployment. All measurements were binned into 2-m bins per segment (a segment is a collection of profiles between surfacing and acquisition by GPS) and assigned a mid-point latitude and longitude.

2.2.1. Oxygen measurements

The Aanderaa Oxygen Optode measures raw phase shifts across a calibrated foil. This instrument, in combination with temperature measurements from the CTD, provides the concentration and saturation percent of dissolved oxygen (DO). The manufacturer calibration and a two-point test (0% and 100% saturation) were performed in the laboratory prior to deployment (Kohut et al., 2014). During post-processing DO data was time shifted backward to account for a 25 s response rate of the foil.

2.2.2. Optical measurements

The Wetlabs ECO-triplet collected chlorophyll-a fluorescence, colored dissolved organic matter (CDOM), and the volume scattering function (VSF) of optical backscatter at a wavelength of 700 nm in the 117° back direction. The VSF measurements are then

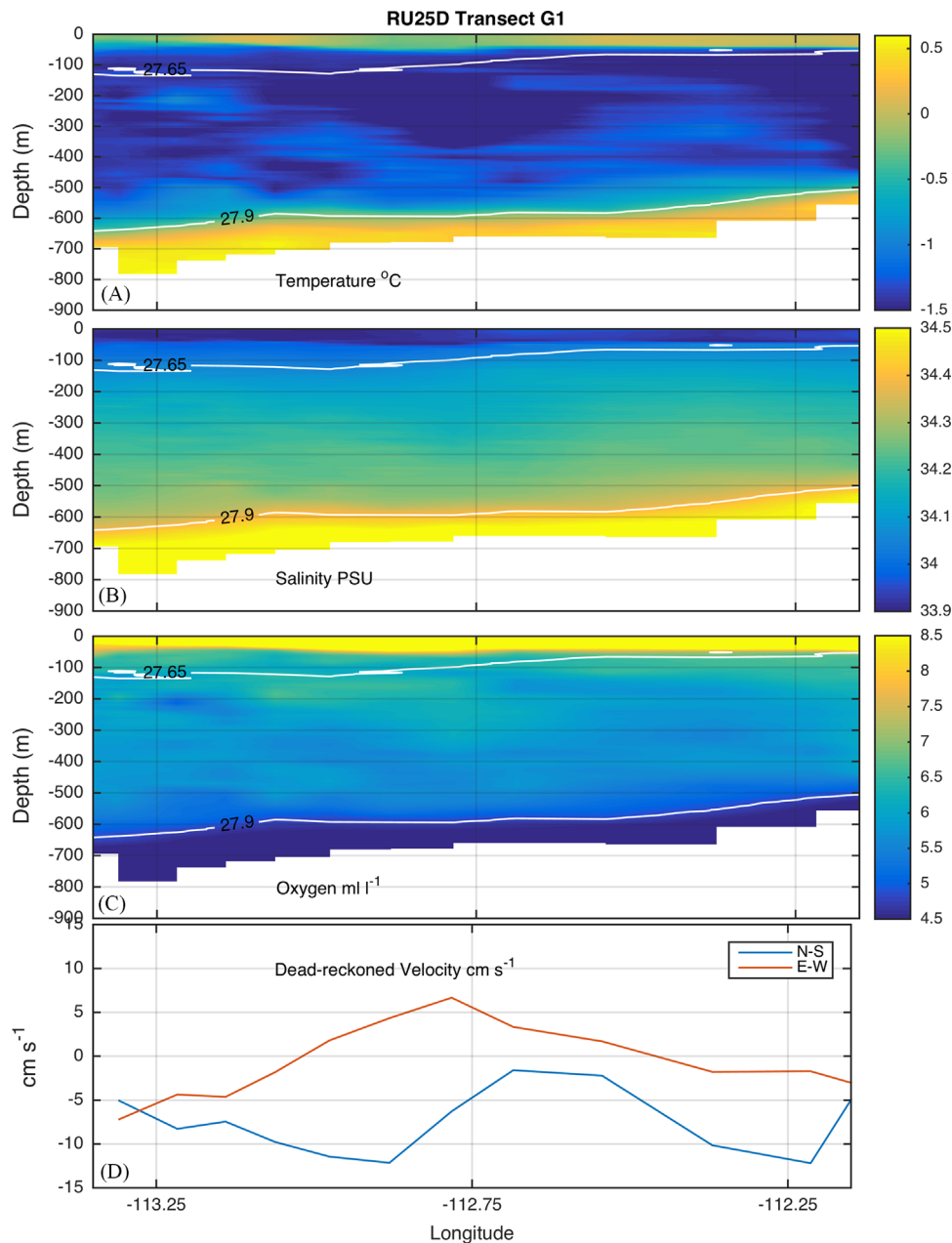


Fig. 3. Cross-sections of (A) temperature, (B) salinity, (C) oxygen, and depth averaged dead-reckoned glider currents along glider transect G1 with longitude along the x-axis. White contours are neutral densities of 27.65 and 27.9 (kg m^{-3}).

converted to backscatter coefficients following [Boss and Pegau, \(2001\)](#) with resultant units of m^{-1} . Optical backscatter responds linearly to suspended particle concentration, but is sensitive to particle size, shape, color, and composition ([Boss and Pegau, 2001](#)). Thus we used these values as a proxy for the relative changes in suspended particle concentration rather than absolute concentration.

2.2.3. Glider velocity calculations

Water velocities were calculated from the glider data using a dead-reckoning technique ([Davis et al., 2003](#)). Glider vertical speeds are derived from the pressure sensor and used in combination with a measured pitch angle to estimate the glider horizontal motion. The initial glider waypoint pre-dive and time integrated estimated horizontal speeds were used to estimate the gliders surfacing position. The difference between the expected and actual surfacing location divided by the total dive time results

in a total depth and time-averaged velocity that we assign to the mid-point of the each pre- and post-dive latitude and longitude. RU25D did not surface frequently enough to resolve tidal currents, but as evidenced by the CATS2008b barotropic tidal model ([Padman et al., 2002](#)) the dominant M2 and S2 tidal currents were relatively small ($< 2 \text{ cm s}^{-1}$) for the duration of the deployment. Potential sources of error in dead-reckoned glider depth and time-averaged velocities have been discussed in detail previously ([Todd et al., 2011](#)) and include uncertainties in angle-of-attack, vertical water velocities, and accumulated errors from integrated measured heading, pitch, and glider vertical velocities. For RU25D heading dependent compass corrections were applied based on pre-deployment calibrations removing a major source of error. Uncertainties from other sources listed above have been found to be typically on the order of 1 cm s^{-1} .

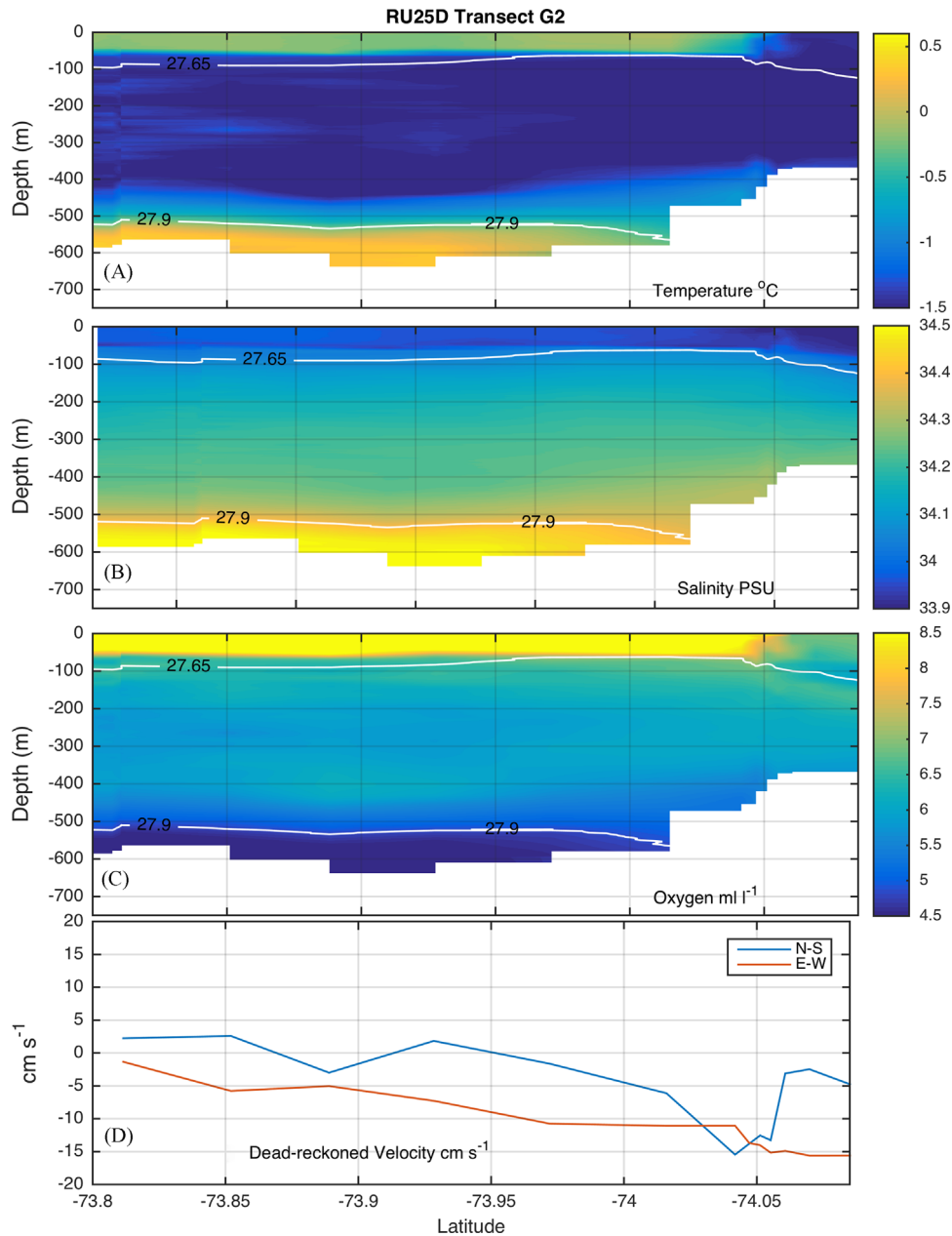


Fig. 4. Cross-sections of (A) temperature, (B) salinity, (C) oxygen, and depth averaged dead-reckoned glider currents along glider transect G2 with latitude along the x-axis. White contours are neutral densities of 27.65 and 27.9 (kg m^{-3}).

2.3. Meltwater concentrations

Meltwater fraction calculations are performed following Jenkins (1999) and Jenkins and Jacobs (2008). This method assumes that the ice-seawater system is closed and that in its simplest form, with only two uniform end-members including a single water mass and ice, the meltwater concentration of a single tracer can be represented as:

$$\frac{Q_i}{Q} = \frac{\chi_w - \chi}{\chi_w - \chi_i} \quad (1)$$

where Q_i is the mass of ice, Q is the total mass represented by $Q = Q_i + Q_w$, Q_w is the mass of seawater, χ is the measured tracer property, and χ_i and χ_w are the tracer properties of the ice and seawater, respectively. Mixtures of meltwater and seawater will have two conservative properties that plot as a straight line on a bivariate graph and the concentration of meltwater can be determined from where

measurements fall on that mixing line. Temperature and salinity are two typical tracers used in this method (Gade, 1979). For our case, and many other realistic cases, there is a third water mass involved, namely Winter Water (WW) that mixes with the CDW-meltwater mixture and further complicates the analysis. In order to address this, a composite tracer approach (McDougall, 1990; Jenkins and Jacobs, 2008) has been developed, where $\psi^{2,1}$ is the composite of two tracers represented by

$$\psi^{2,1} = (\chi^2 - \chi_{CDW}^2) - (\chi^1 - \chi_{CDW}^1) \left(\frac{\chi_{WW}^2 - \chi_{CDW}^2}{\chi_{WW}^1 - \chi_{CDW}^1} \right), \quad (2)$$

which is the difference between the measured value of an additional tracer, such as oxygen, and the idealized two component mixture mentioned above. The resultant meltwater fraction is then the ratio of the mixture composite tracer $\psi_{mix}^{2,1}$, to the meltwater $\psi_{melt}^{2,1}$. The method is described in more detail in Jenkins (1999) and Jenkins and Jacobs (2008).

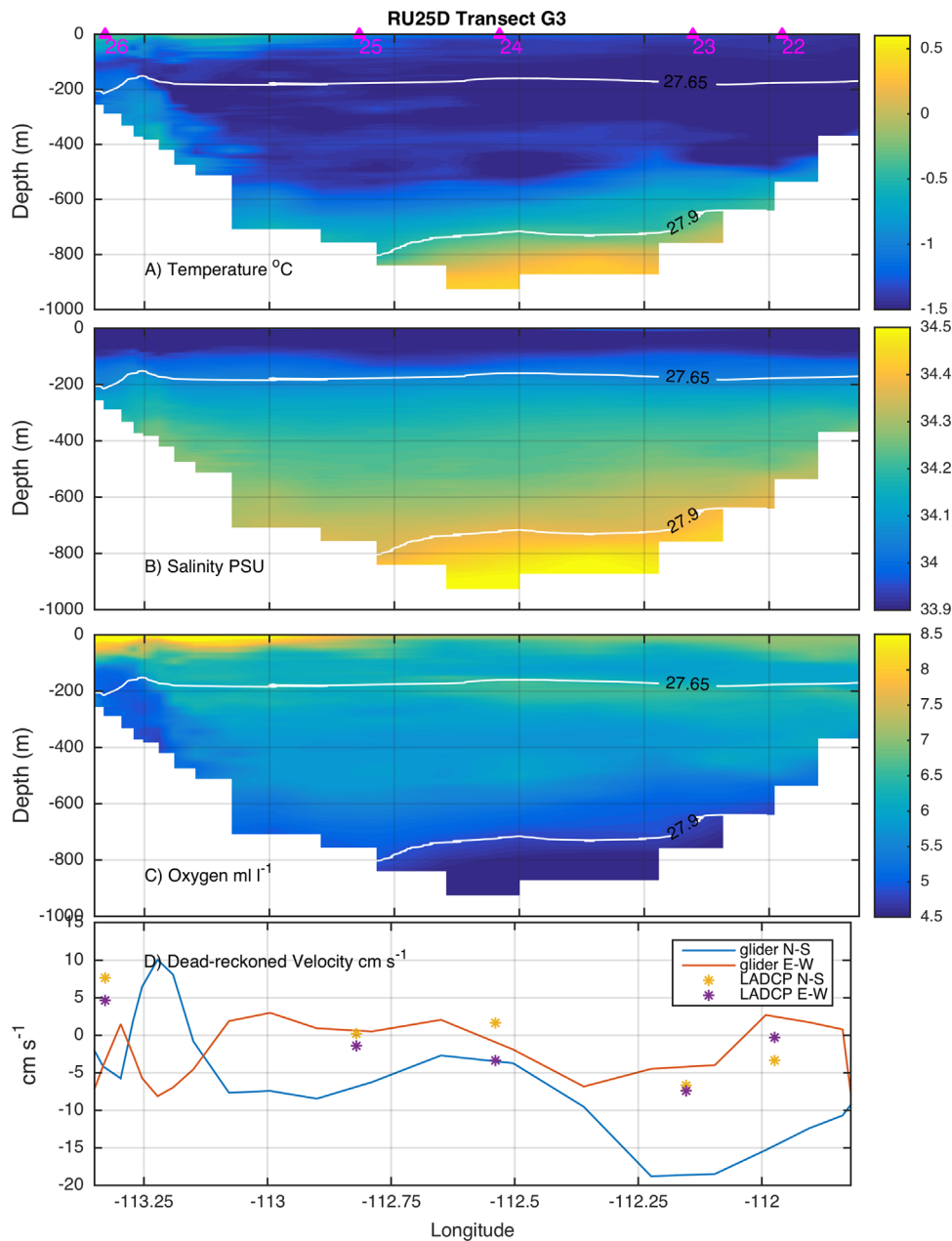


Fig. 5. Cross-sections of (A) temperature, (B) salinity, (C) oxygen, and (D) depth averaged dead-reckoned glider currents (lines) and depth averaged LADCP currents (stars) along glider transect G3 with longitude along the x-axis. Ship sampling locations are plotted along the top of Fig. 5A (magenta triangles) with numbers corresponding to the right panel of Fig. 1. White contours are neutral densities of 27.65 and 27.9 (kg m^{-3}).

The tracers used here are salinity, potential temperature, and dissolved oxygen. Outside of the surface layers where atmospheric properties influence these tracers there are distinct end members for WW, CDW, and glacial ice in the Amundsen Sea (Jenkins and Jacobs, 2008). Based on the ambient water masses observed on the Amundsen Sea continental shelf in 2014 we use an mCDW end-member derived from the maximum temperature and salinity measured by the glider in the Dotson Trough and its associated oxygen concentration with $T \sim 0.5^\circ\text{C}$, $S \sim 34.55$ PSU, and $\text{O}_2 \sim 4.2 \text{ ml l}^{-1}$; WW derived from the minimum temperature on the shelf with properties $\sim -1.7^\circ\text{C}$, $S \sim 34.23$ PSU, and $\text{O}_2 \sim 6.15 \text{ ml l}^{-1}$ (Fig. 2b); and theoretical ice properties $T \sim -90.75^\circ\text{C}$, $S \sim 0$ PSU, and $\text{O}_2 \sim 28.46 \text{ ml l}^{-1}$. These ice values are derived from past studies in the Amundsen Sea (Hellmer et al., 1998; Jenkins, 1999; Jenkins and Jacobs, 2008), with temperature values representative

of losses in the phase change from ice to liquid water. Oxygen values within the ice are drawn from oxygen concentrations within air pockets in the ice, which are forced entirely into solution when ice melts at the pressures beneath the ice sheet. Meltfractions are reported as the mean of the three independent meltfraction $T-S$, O_2-S , and O_2-T pairs. Standard deviations were calculated across all three pairs for each measured bin and values greater than one quarter of the theoretical upper bound of expected meltwater fractions were flagged and not included in the analysis. This occurred primarily in the upper mixed-layer where the calculations are unreliable due to the influence of air-sea exchanges on water properties.

In addition to calculating meltfractions using the above method, we also use the Gade line (Gade, 1979), a line of constant mixing between the ice and ocean water, to visualize meltwater in

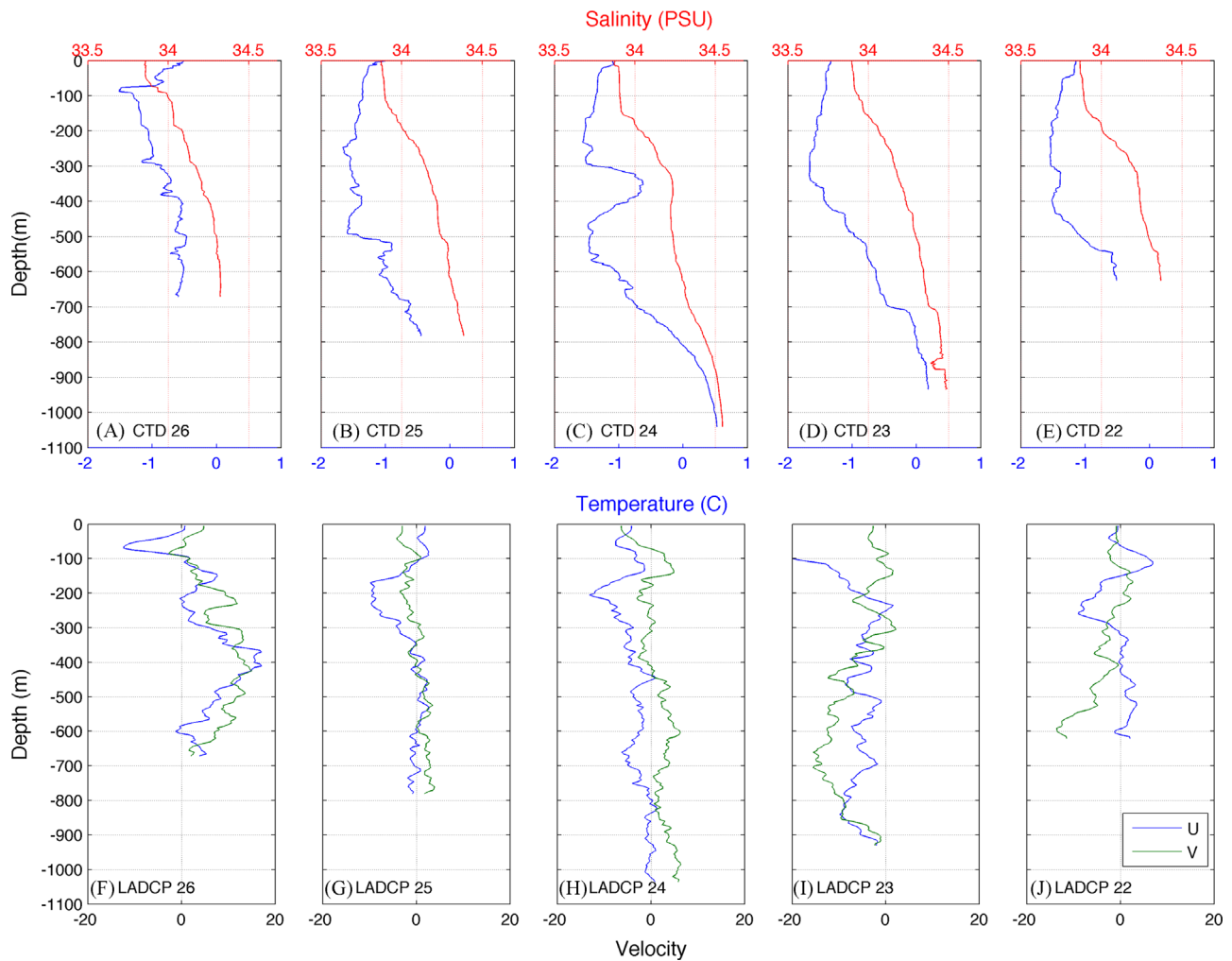


Fig. 6. Profiles of (A)–(E) IBRV *Araon* temperature (blue) and salinity (red) and (F)–(J) LADCP east-west (blue U) and north-south (green V) velocity at the locations indicated in Figs. 5A and 1B.

T – S space. The Gade line is represented by the equation:

$$T_p(S_p) = T_{ocean} + \frac{L_f}{C_p} \left(1 - \frac{S_{ocean}}{S_p} \right) \quad (3)$$

where T_{ocean} and S_{ocean} are the ocean end-members prior to melting, in this case mCDW end-members listed above. L_f is the latent heat of fusion for ice (334 kJ kg^{-1}); and C_p is the specific heat of water (3.97 kJ kg^{-1}) at salinity of 34.7 PSU, temperature of 1°C , and pressure of 400 dbar.

3. Results

In January 2014 the Amundsen Sea continental shelf had three major water masses present (Fig. 2); i.e. Antarctic Surface Water (AASW) ($T > 0^\circ \text{C}$, $S < 34$ PSU), Winter Water (WW) ($T \sim -1.8^\circ \text{C}$, $S \sim 34.2$ PSU), and mCDW ($T \sim 0.5^\circ \text{C}$, $S \sim 34.55$ PSU). Pure CDW ($T > 1.5^\circ \text{C}$, $S > 34.5$ PSU) was observed in ship-borne CTD profiles off the shelf, and was not present in the Dotson Trough.

RU25 traveled across the Dotson Trough from east to west (transect G1) on January 4th 2014 (Fig. 1B). Along this transect warm (0.5°C), salty (34.5 PSU) mCDW was observed leaning on the eastern flank of the trough (Fig. 3) consistent with along-isobath southward flow observed in previous studies (e.g. Wählin et al., 2010; Ha et al., 2014). Oxygen concentrations in the warm layer were below 5 ml l^{-1} , with minimum values of 4.2 ml l^{-1}

near 800 m. dead-reckoned depth and time-averaged velocities are shown in Fig. 3D, with primarily southward velocities exceeding 5 cm s^{-1} for the majority of the transect, with minimum values near 0 cm s^{-1} at 112.75°W . The velocity minimum in the center of the transect coincides with a region where the glider track runs parallel to curving bathymetry between 112.8 and 112.4°W (Fig. 1B), so the current likely continued along-isobath although the direction changed.

RU25D was turned southward on January 6th, 2014 and traveled along the 600 m isobath toward the DIS (transect G2), along the ridge separating the Dotson from the Crosson basin. Temperature, salinity, and oxygen (Fig. 4) in the near bottom mCDW layer was uniformly distributed near bottom from north to south between 73.8 and 74°S indicating limited interaction and mixing with overlying WW on the eastern side of the Dotson Trough. There was a persistent westward velocity increasing with proximity to DIS up to 10 cm s^{-1} , consistent with a coastal current that flowed along the DIS (Figs. 1B and 4D). RU25D was briefly piloted nearshore into shallower waters of ~ 400 m depth, just offshore of the Bear Peninsula. The velocity there showed a stronger westward current component, and the hydrography a significantly cooler ($< -1.5^\circ \text{C}$), fresher (< 33.9 PSU), and less oxygen rich ($< 7 \text{ ml l}^{-1}$) surface water. No mCDW was present near the bottom in this region (Fig. 4), indicating that the mCDW remained at depth and continued along-isobath deeper than 400 meters.

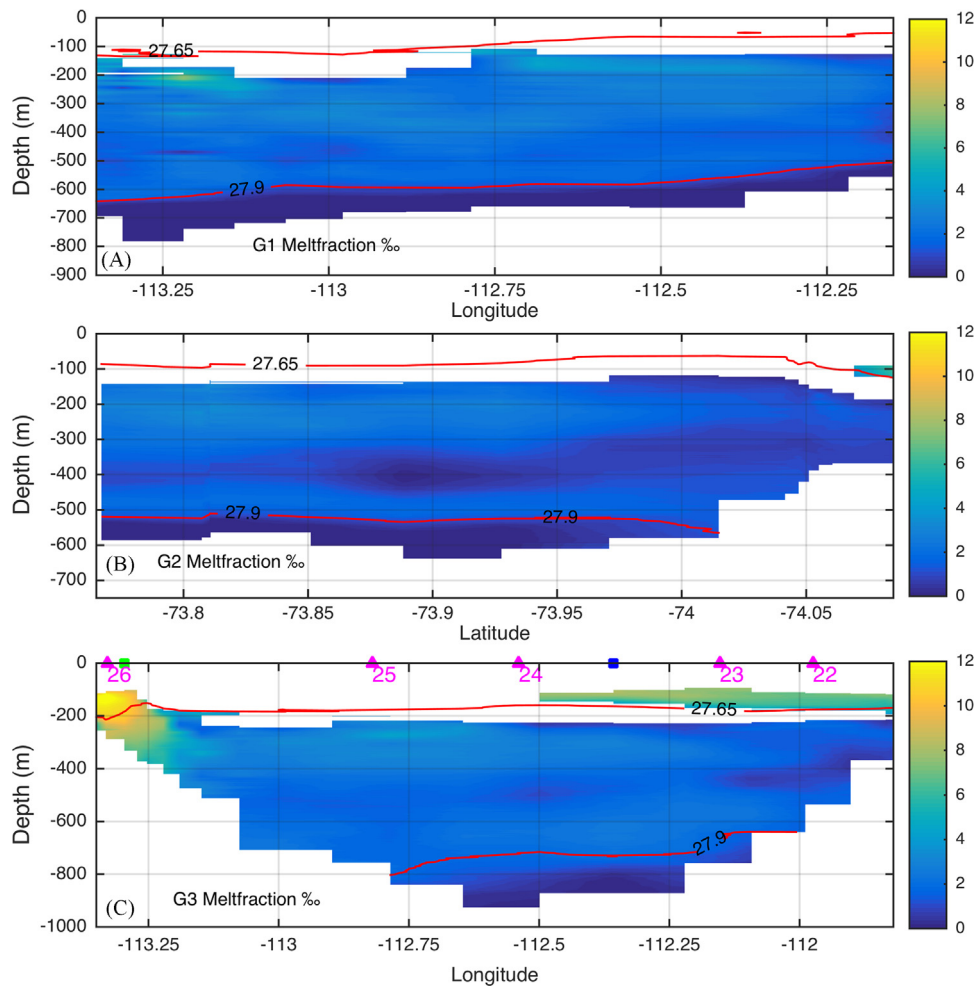


Fig. 7. Meltwater fraction cross-sections corresponding to 7A) transect G1, 7B) transect G2, and 7C) transect G3. Ship sampling locations are plotted along the top of 7C (magenta triangles) with numbers corresponding to the Fig. 1B and profiles in Fig. 6. Surface values where the three tracer pair meltwater fractions exceeded two standard deviations were removed as they are likely not valid due to atmospheric input. Red contours are neutral densities of 27.65 and 27.9 (kg m^{-3}).

3.1. Dotson Ice Shelf inflow

On January 8th, 2014 RU25D performed a cross-trough transect near the ice shelf front, G3 (Figs. 1B and 5), toward the west from the edge of the Bear Peninsula to within 8 km of the Martin Peninsula. The glider remained within 6 km of the DIS until ice conditions to the west forced RU25D to be piloted toward the northwest. Additionally, five CTD and LADCP stations (22 through 26) were performed by the IBRV *Araon* along the DIS within a few kilometers south of the glider track (Figs. 1B and 6). In similarity with the cross-trough glider section further north, the mCDW layer is spread on the eastern flank of the trough (Fig. 5). The shipboard profiles (Fig. 6) at stations 22 through 25 show similar characteristics as glider profiles with the warmest (> 0.5 °C) and saltiest waters at station 24 (> 34.55 PSU). However many of the fine-scale features are naturally lacking in the CTD transect, in particular the pronounced cold and fresh core seen at the bottom to the east of station 26. Oxygen concentrations in the central trough were less than 4.5 ml l^{-1} consistent with upstream values of mCDW along transects of G1 and G2. The 27.9 kg m^{-3} contour in all three transects (Figs. 3A, 4A, and 5A) shows that the near bottom layer is consistent throughout the trough and suggests that there was limited mixing of the core mCDW near the bottom with overlying WW prior to entering into the ice shelf cavity. A strong (up to 20 cm/s) southward flow toward the ice shelf cavity can be

seen over the eastern part of the transect (Fig. 5D) where weaker currents (near 5 cm s^{-1}) were present in the central portion of the trough. Ship-borne LADCP profiles at stations 22 and 23 show detided southward velocities below 200 m depth to the bottom with maximum values over 15 cm s^{-1} at 600 m in station 22 and at 700 m depth in station 23 (Fig. 6). At station 24 near the bottom within the mCDW layer velocities were near $\sim 5 \text{ cm s}^{-1}$ northward. Depth averaged LADCP velocities on the eastern flank of the Dotson Trough showed weaker ($\sim 7 \text{ cm s}^{-1}$) southward flow than glider measurements near the same location (Fig. 5D). If shipboard data is considered on its own, this would suggest that the waters flowing toward and beneath the DIS were limited to the slightly weaker mCDW signature at stations 22 and 23, though based on glider dead-reckoned currents and hydrographic observations there is still significant southward flow between stations 23 and 24 where mCDW presence remains high.

3.2. Dotson Ice Shelf outflow

On the western flank of the trough, west of 113.2°W there is a distinct water mass with elevated temperature and salinity and reduced oxygen relative to other water masses between 100 and 500 meters depth. Temperatures within this water mass ranged from -0.5 to -1.3 °C. Salinities were between 34 and 34.25 PSU. The signal is most clearly seen in the oxygen data; with oxygen

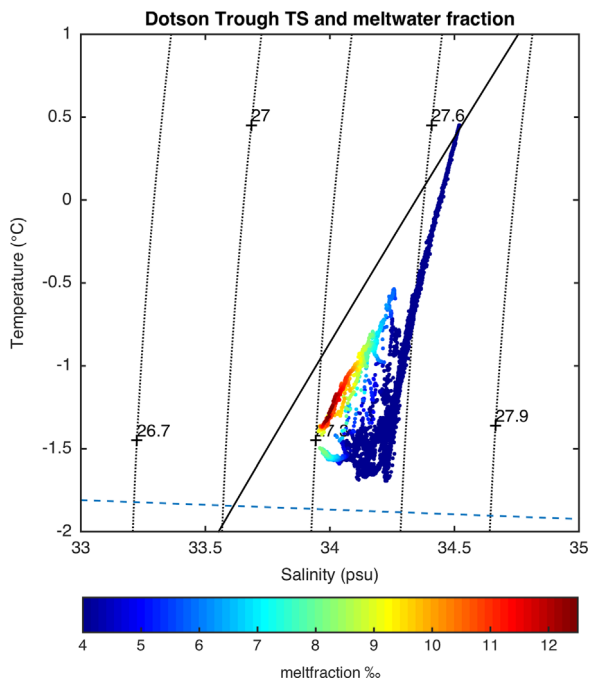


Fig. 8. Temperature and salinity diagram with meltwater fraction plotted in colors. The blue dashed line indicates the freezing point of seawater and the black solid line is the Gade Line (Gade, 1979) with end members of -0.5°C and 34.55 PSU and for ice -90.75°C and 0 PSU (Hellmer et al., 1998).

values between 5 and 5.5 ml l^{-1} standing in stark contrast to the oxygenated AASW and WW. Dead-reckoned glider velocities show northward flow of up to 10 cm s^{-1} coinciding with this water mass, indicating that this is a northward flowing jet focused on the steep bathymetry of the western flank of the DIS trough. While the CTD data at station 26 did not capture the main outflow clearly, the LADCP data does show northward velocities between 100 and 700 m, with peak values of near 20 cm s^{-1} at 400 m, just below the core depth of the outflow region in the glider data. Depth-averaged LADCP velocities were northward at $\sim 8\text{ cm s}^{-1}$ and compared well with glider velocities (Fig. 5D), though they were shifted westward as the glider sampled a more northerly location where bathymetry curved toward the east (Fig. 1B).

3.3. Meltwater fraction

Meltwater fractions for transects G1, G2, and G3 are all shown in Fig. 7, with the highest values of over 12 parts per thousand found on the western portion of G3. The lowest meltwater fractions are evident in the near bottom regions of G1, G2, and the inflow region of G3 between 112.75 and 112.20°W . The low values of G1, G2, and the inflow region of G3 indicate little mixing with the overlying WW along the trough. When plotted as a scatter plot in T - S space, along with the Gade Line (Gade, 1979), it can be seen that the meltwater falls below and parallel to the Gade Line with end members presented above (Fig. 8). This indicates that for the current time period WW is either further mixed with mCDW prior to inducing melt or mixed with outflowing meltwater before being sampled by the glider.

3.4. Optical properties

As mentioned above, optical backscatter serves as a proxy for suspended particle concentration in the water column. Values in

the uppermost 50 m within the AASW layer on transects G1, G2, and G3 are elevated with values of consistently over 0.01 m^{-1} (Fig. 9). These surface values are highest further away from the glacial face along transect G1 and are most likely related to the high biomass associated with a large chlorophyll bloom away from the shelf. Chlorophyll values recorded by the glider were in excess of 25 mg m^{-3} along transect G1 and G2 and were much lower with proximity to the DIS in transect G3 (Fig. 10b). Winter water in all three transects has the lowest optical backscatter values, while near bottom values in the mCDW are approximately an order of magnitude greater than WW. Optical backscatter generally increases toward the bed indicating a possible sedimentary source of particles with near bottom maxima of $\sim 0.001\text{ m}^{-1}$ for sections G1, G2, and the portion of G3 east of 112.8°W that is associated with the Dotson Trough inflow.

Meltfractions greater than 1 parts per thousand and optical backscatter have a linear relationship (Fig. 11A) with R^2 of 0.657, which suggests that suspended particulate matter is sourced from glacial melt water in the outflow region. Fig. 12 shows the lower 100 m of two optical and meltfraction profiles from the inflow and outflow regions. The western outflow region of G3 has near-bottom values of optical backscatter of about $\sim 0.001\text{ m}^{-1}$, nearly equal to the near-bottom values in the inflow but in contrast to the inflow region optical backscatter increases with distance from the bed, indicating an overlying particle source. There are two distinct regions where meltfractions increase and optical backscatter does not represented in blue and green in Fig. 11A. Both of these regions have neutral densities of less than 27.65 kg m^{-3} (Fig. 7). The first peak has an optical backscatter of $\sim 0.0006\text{ m}^{-1}$ and meltwater fractions between 4 and 8 parts per thousand, while the second peak has an optical backscatter of $\sim 0.00125\text{ m}^{-1}$ and meltfraction between 8 and 13 parts per thousand.

4. Discussion

Observations of the pathways of warm mCDW and glacial meltwater beneath ice shelf cavities are limited. Yet, the evolving circulation is critical to understanding how climate shifts will affect physical and biogeochemical processes in the highly productive polynya waters close to these cavities (Arrigo et al., 2012; Lee et al., 2012; Yager et al., 2012). Previous field campaigns have used a handful of individual ship-based profiles to identify inflow and outflow regions along Pine Island Glacier (Jenkins et al., 2010; Jacobs et al., 2011; Dutrieux et al., 2014), the DIS (Randall-Goodwin, 2012; Yager et al., 2012), and other systems (Jenkins and Jacobs, 2008). Traditional CTD transects would collect at best only a few profiles in outflow regions, and often miss them all together. For example, in the 2014 ANA04B cruise just one profile (station 26) was located on the western flank of the DIS, and it did not capture the core or the vertical and horizontal spatial extent of the main outflow.

As described by Ha et al. (2014), past studies have found the outflow on the western flank of the Dotson Trough to account for approximately 1/3 of the inflow. Using the width and height of the 27.9 kg m^{-3} neutral density contour from the bed and glider depth-averaged velocities we obtain an inflow estimate of $\sim 0.39\text{ Sv}$. This is slightly larger but on the same order of magnitudes as inflow estimates by Ha et al. (2014).

RU25 collected 15 profiles within the outflow region. At the time this outflow extended approximately 7 km from the 500 m isobaths to inshore of the 200 m isobaths. Using the glider sampled bathymetry, the 27.6 kg m^{-3} neutral density contour, the 7 km width of the outflow, and the depth and time-averaged velocities within the outflow we estimate a northward transport of $\sim 0.06\text{ Sv}$ ($1.9 \times 10^{12}\text{ m}^3\text{ yr}^{-1}$). With an average meltwater fraction

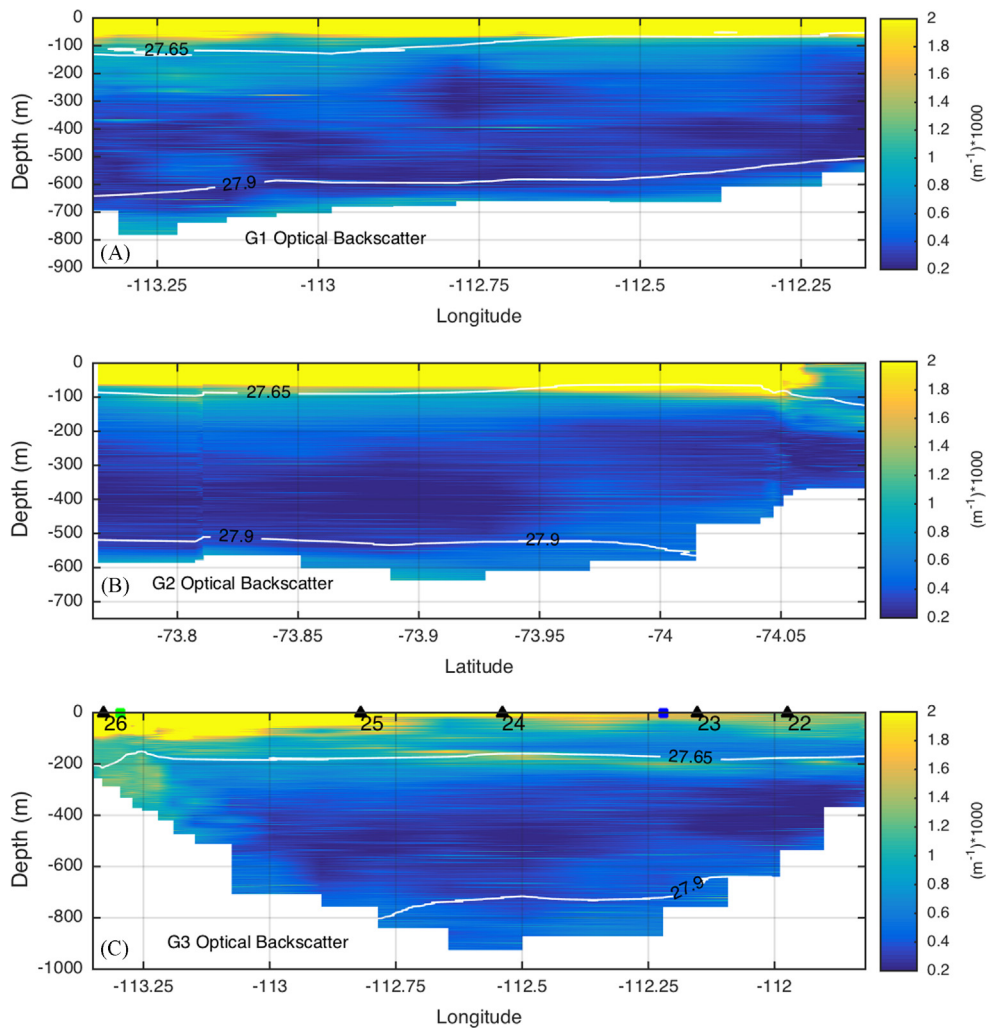


Fig. 9. Optical backscatter cross-sections corresponding to 9A) transect G1, 9B) transect G2, and 9C) transect G3. Ship sampling locations are plotted along the top of 9C (black triangles) with numbers corresponding to the right panel of Fig. 1 and profiles in Fig. 6. Blue and Green squares correspond to the glider profiles plotted in Fig. 12, with the Blue representing the inflow region and green representing the outflow region. White contours are neutral densities of 27.65 and 27.9 (kg m^{-3}).

of $\sim 1\%$ this equates to $1.9 \times 10^{12} \text{ m}^3 \text{ yr}^{-1}$ of meltwater in the DIS outflow, or $\sim 19 \text{ Gt yr}^{-1}$. This is less than instantaneous estimate of 81 Gt yr^{-1} from the 2011 ASPIRE cruise (Randall-Goodwin et al., 2015) and the 5-year average of 42 Gt yr^{-1} from Rignot et al. (2013), but likely reflects high seasonal and interannual variability in the region. While this value is uncertain due to the usage of glider depth and time-averaged velocities, a similar result using ship based methods would require extensive and focused LADCP profiling in this region, which is costly and not feasible due to the remote nature of the region. Furthermore, future modeling efforts will need to have resolutions that can capture the narrow width of the outflow in order to accurately represent the DIS outflow.

Among other environmental factors such as light availability, macronutrient supply, and upper mixed layer depth Fe has been identified as a necessary micronutrient to support large phytoplankton blooms in the ASP (Arrigo and van Dijken, 2003; Arrigo et al., 2008; Smith and Comiso, 2008). Recent studies have identified high levels of Fe in meltwater near the DIS (Alderkamp et al., 2015) and significant concentrations have been observed as far as 150 km from the Pine Island Glacier (Gerringa et al., 2012). Fe has been hypothesized to originate from a number of sources including basal melt of the sediment laden ice shelf or sub-glacial sediment resuspension from the bed.

While no direct observations of Fe are possible from the gliders, optical backscatter can serve as a proxy of suspended particulate matter. Not all particulate matter may contribute to Fe concentrations, but particulate Fe has been observed near the DIS and found to be important for the ASP. The glider based optical backscatter measurements increase logarithmically toward the bottom for the eastern (inflow) region. This is known as a Rousian sediment distribution and is typical of resuspended sediment on continental shelves (Grant and Madsen, 1986; Glenn and Grant, 1987; McLean, 1991; Madsen et al., 1993). In semi-log space, as in Fig. 12, Rousian profiles increase linearly toward the bed. The distribution is a result of the balance between the turbulence generated from the current shear within the bottom boundary layer that acts to keep sediment in suspension and gravitational forces, which cause sediment particles to fall out of suspension. A reduction in shear away from the bed leads to reduced turbulence and a smaller sediment concentration. Unlike the inflow region, the outflow region optical backscatter profile is non-Rousian (Fig. 12b). The fact that the optical backscatter increases with distance above the bottom in the glacial meltwater outflow indicates an external source of particles to the water column.

There are two regions where meltwater concentration increases but optical properties remain constant (Fig. 12) suggesting that some portion of the DIS is not sediment laden and contributes minimally

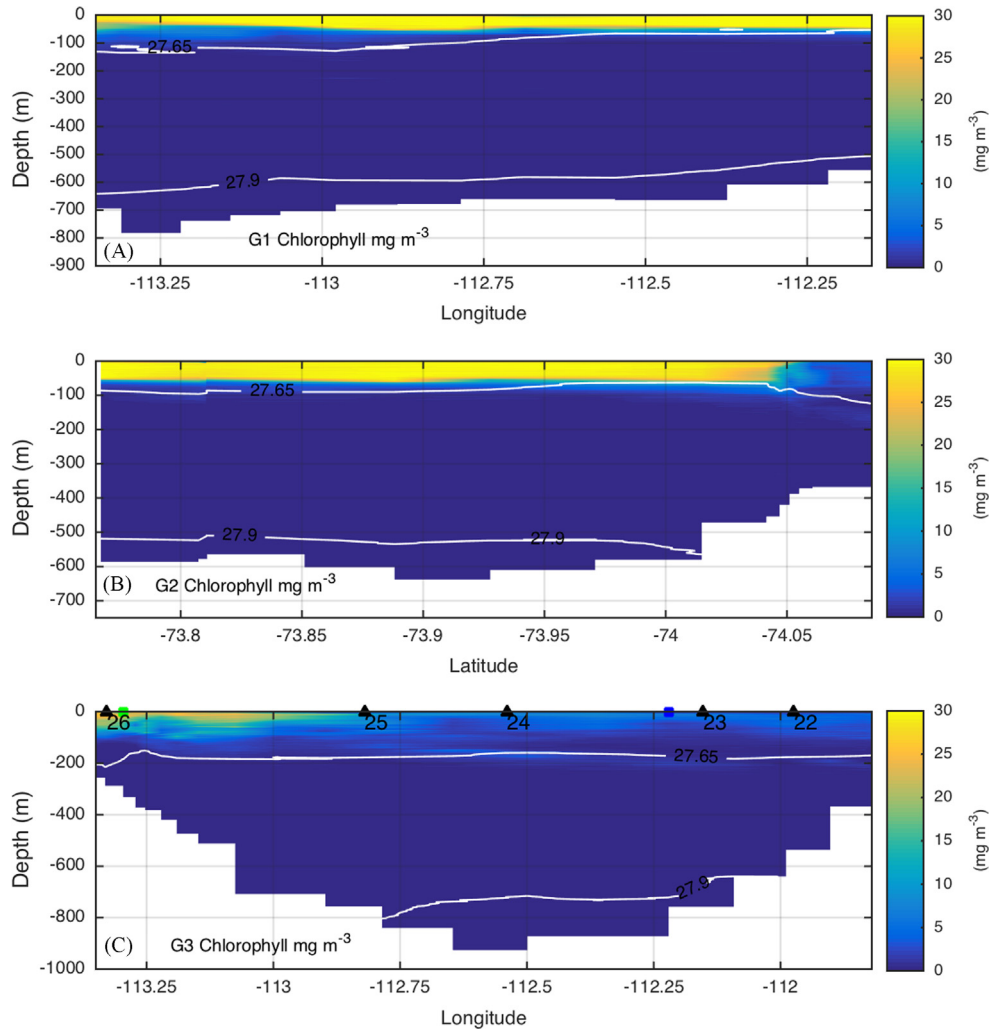


Fig. 10. Chlorophyll concentration cross-sections corresponding to 10A) transect G1, 10B) transect G2, and 10C) transect G3. Ship sampling locations are plotted along the top of 9C (black triangles) with numbers corresponding to the right panel of Fig. 1 and profiles in Fig. 6. Blue and Green squares correspond to the glider profiles plotted in Fig. 12, with the Blue representing the inflow region and green representing the outflow region. White contours are neutral densities of 27.65 and 27.9 (kg m^{-3}).

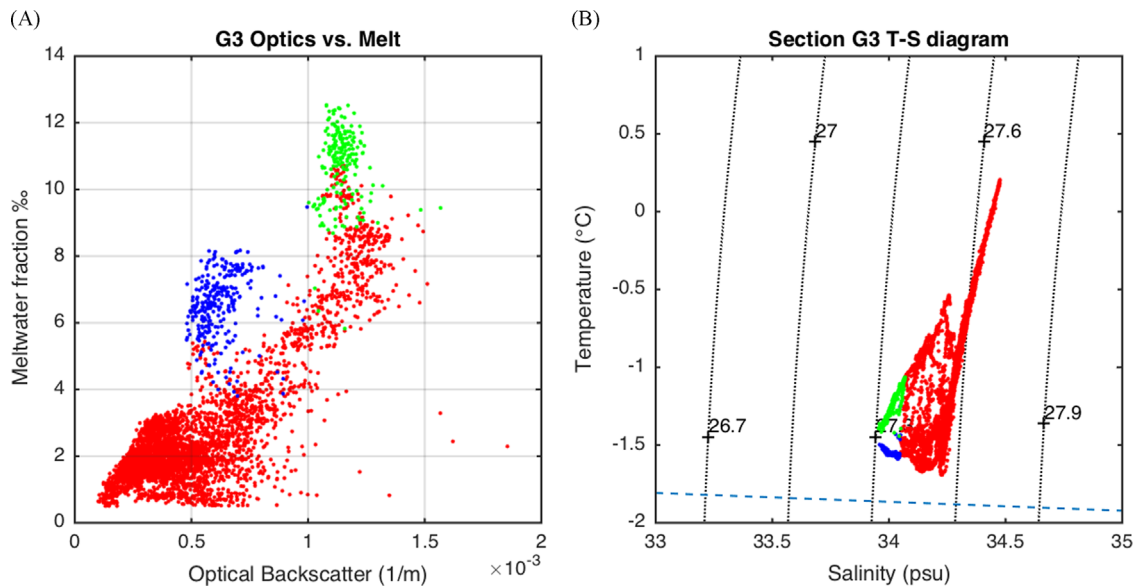


Fig. 11. (A) plot of meltwater fraction (y-axis) vs. optical backscatter (x-axis) and (B) T-S diagram of the data from panel A. Blue and green points represent regions where meltwater fractions increase independent of optical backscatter.

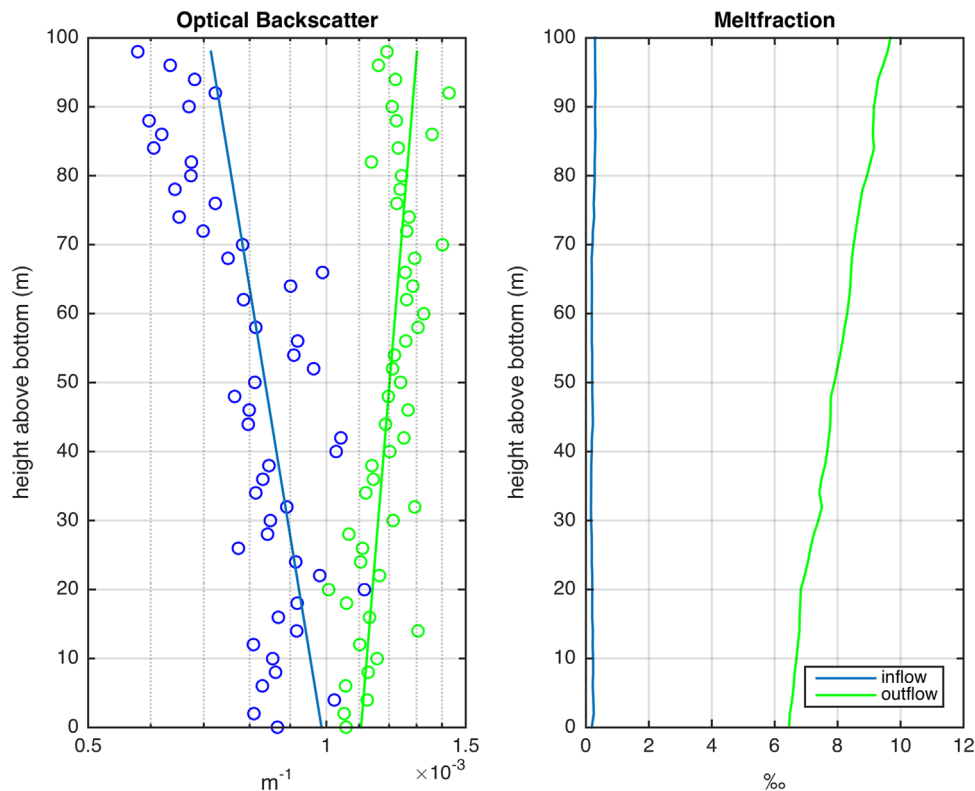


Fig. 12. (Left panel) Profiles of optical backscatter on a semi-logarithmic x scale and (right panel) meltwater fraction with the y-axis for both corresponding to height above bottom. Blue lines represent the inflow and green represent the outflow at locations denoted by the Blue and Green squares in Fig. 9C.

to the suspended particle concentration. In T - S space (Fig. 11B) the first peak (blue) with low optical backscatter is closely related to WW, indicating a region where WW reached the ice-shelf face near 150 meters depth (above the 27.65 kg m^{-3} contour in Fig. 7) on the eastern flank of the trough. Observations from the 2011 ASPIRE (Yager et al., 2012) cruise show the ice shelf draft on the eastern flank was at approximately 200 meters (Randall-Goodwin, 2012) depth, supporting this finding. The second peak (green) coincides with the region running parallel to the Gade line (Fig. 8) indicating that the same water mass that induced suspended particle laden melt also interacted with ice that made a limited particle contribution. One potential explanation for this is that buoyant meltwater rises up along the ice shelf base and induces further melt in the shallower part of the cavity close to the ice shelf edge where the ice may have lower sediment concentrations.

Aside from the two regions mentioned above, the nearly linear relationship between optical backscatter and meltwater fraction (Figs. 11 and 12b) points to glacial meltwater as the primary source of particles and the existence of a muddy ice shelf base inland of the grounding zone. This has implications for the flow speed of the grounded ice and also indicates that glaciers can serve as an important source of Fe to the water in this region. Detailed marine geological surveys and dating of the sediments (Smith et al., 2014) indicate that the ice sheet base has been sediment-laden for the last 20,000 years as it retreated across the ASE. Elevated optical and meltwater fraction signatures were also observed offshore near 113.25°W and 73.72°S in transect G1 at 200 m (Figs. 7 and 8). This is nearly 35 km north of the outflow and indicates that the particle heavy outflow waters continue northward toward the central ASP, and are not limited to the nearshore coastal zone consistent with glider observations of the phytoplankton blooms in the 2010–2011 field year (Schofield et al., in press). This is also consistent with the observations of meltwater-rich outflows near

the outer shelf (Wählin et al., in press; Ha et al., 2014); i.e. observations that at least a third of the outflow makes it back to the outer shelf.

Past studies have indicated that the phytoplankton bloom in the ASP also has strong interannual variability (Arrigo and van Dijken, 2003). The intrusion of CDW into the Dotson Trough, while persistent (Arneborg et al., 2012) has significant interannual variability in the thickness and temperature (Assmann et al., 2013). The limited multi-year observations (Wählin et al., in press; Wählin et al., 2013; Ha et al., 2014) show a strong annual and interannual variability of CDW intrusion along the deep troughs, which presumably reflects on the circulation beneath the Dotson Ice Shelf, and subsequently to the supply of Fe to the ASP. This modulation of the Fe-supply could potentially account for variability in size and duration of the ASP summer and spring blooms.

5. Conclusions

In this study we used a Teledyne-Webb Slocum glider to obtain high spatial and temporal resolution oceanographic data along the front of DIS in the ASP. With the glider RU25D, a narrow ($\sim 7 \text{ km}$) outflow of glacial meltwater was identified on the western flank of the DIS, a feature nearly missed in the ship based profiles due to too large spacing between stations. The outflow was northward flowing, had high meltwater fractions, and elevated optical backscatter. The shape of the optical backscatter profiles and their high correlation with meltwater fraction indicate that particles in the outflow were primarily sourced from basal melt of the DIS, not resuspended sediments. This suggests that the DIS originates in a sediment-rich ice sheet base inland of the grounding zone, that particulate Fe previously found in the region is likely of glacial origin, and that its interannual variability could potentially be linked to the size and duration of CDW

intrusions onto the shelf. In order to confirm this result future studies should target the DIS outflow, examination of the Kohler glacier base, and use a combination of ship-based profiles, moorings, and autonomous underwater vehicles to track the properties and fate of this outflow as it moves northward toward the central polynya. By leveraging glider systems to take over hydrographic survey responsibilities research vessels could be better focused on process-based studies in regions of interest and perform mooring recovery and deployment activities while increasing data density in these difficult to access, yet climate critical, regions of interest.

Acknowledgments

The authors acknowledge the Korea Polar Research Institute for its support and funding from Grant programs (PP14020 and PP15020), Teledyne-Webb graduate fellowship for graduate student funding, the Rutgers University Center for Ocean Observing Leadership for glider piloting and support, and the dedication and support of the crew and scientists of the IBRV Araon. Inha University research Grant (INHA-51416) supported Ho Kyung Ha. We would also like to thank Pierre Dutrieux for scientific codes and commentary on many of the draft figures. Additionally, we thank the two anonymous reviewers for the helpful and thoughtful comments that greatly improved this paper.

References

- Adams, K.A., Barth, J.A., Chan, F., 2013. Temporal variability of near-bottom dissolved oxygen during upwelling off central Oregon. *J. Geophys. Res. Ocean.* 118 (10), 4839–4854. <http://dx.doi.org/10.1002/jgrc.20361>.
- Alderkamp, A.-C., et al., 2012. Iron from melting glaciers fuels phytoplankton blooms in the Amundsen Sea (Southern Ocean): Phytoplankton characteristics and productivity. *Deep Sea Res. Part II Top. Stud. Oceanogr.* 71–76, 32–48. <http://dx.doi.org/10.1016/j.dsr2.2012.03.005>.
- Alderkamp, A.-C., et al., 2015. Fe availability drives phytoplankton photosynthesis rates during spring bloom in the Amundsen Sea Polynya, Antarctica. *Elem. Sci. Anthr.* 3, 000043. <http://dx.doi.org/10.12952/journal.elementa.000043>.
- Arneborg, L., Wählin, A.K., Björk, G., Liljebladh, B., Orsi, A.H., 2012. Persistent inflow of warm water onto the central Amundsen shelf. *Nat. Geosci.* 5 (12), 876–880. <http://dx.doi.org/10.1038/ngeo1644>.
- Arrigo, K.R., van Dijken, G.L., 2003. Phytoplankton dynamics within 37 Antarctic coastal polynya systems. *J. Geophys. Res.* 108 (C8), 3271. <http://dx.doi.org/10.1029/2002JC001739>.
- Arrigo, K.R., van Dijken, G.L., Bushinsky, S., 2008. Primary production in the Southern Ocean, 1997–2006. *J. Geophys. Res.* 113 (C8), C08004. <http://dx.doi.org/10.1029/2007JC004551>.
- Arrigo, K.R., Lowry, K.E., van Dijken, G.L., 2012. Annual changes in sea ice and phytoplankton in polynyas of the Amundsen Sea, Antarctica. *Deep Sea Res. Part II Top. Stud. Oceanogr.* 71–76, 5–15. <http://dx.doi.org/10.1016/j.dsr2.2012.03.006>.
- Assmann, K.M., Jenkins, A., Shoosmith, D.R., Walker, D.P., Jacobs, S.S., Nicholls, K.W., 2013. Variability of Circumpolar Deep Water transport onto the Amundsen Sea continental shelf through a shelf break trough. *J. Geophys. Res. Ocean.* 118 (12), 6603–6620. <http://dx.doi.org/10.1002/2013JC008871>.
- Boss, E., Pegau, W., 2001. Relationship of light scattering at an angle in the backward direction to the backscattering coefficient. *Appl. Opt.* 40 (30), 5503. <http://dx.doi.org/10.1364/AO.40.005503>.
- Boyd, P.W., 2002. Modelling regional responses by marine pelagic ecosystems to global climate change. *Geophys. Res. Lett.* 29 (16), 1–4. <http://dx.doi.org/10.1029/2001GL014130>.
- Castelao, R., Glenn, S., Schofield, O., 2010. Temperature, salinity, and density variability in the central Middle Atlantic Bight. *J. Geophys. Res.* 115 (C10), C10005. <http://dx.doi.org/10.1029/2009JC006082>.
- Chavanne, C.P., Heywood, K.J., Nicholls, K.W., Fer, I., 2010. Observations of the Antarctic slope undercurrent in the Southeastern Weddell Sea. *Geophys. Res. Lett.* 37, 3–7. <http://dx.doi.org/10.1029/2010GL043603>.
- Davis, R., Eriksen, C., Jones, C., 2003. Autonomous buoyancy-driven underwater gliders. In: Griffiths, G. (Ed.), *Technology and Applications of Autonomous Underwater Vehicles*. Taylor and Francis, p. 37.
- Dutrieux, P., De Rydt, J., Jenkins, A., Holland, P.R., Ha, H.K., Lee, S.H., Steig, E.J., Ding, Q., Abrahamsen, E.P., Schröder, M., 2014. Strong sensitivity of Pine Island ice-shelf melting to climatic variability. *Science* 343 (6167), 174–178. <http://dx.doi.org/10.1126/science.1244341>.
- Gade, H.G., 1979. Melting of ice in sea water: a primitive model with application to the antarctic ice shelf and icebergs. *J. Phys. Oceanogr.* [http://dx.doi.org/10.1175/1520-0485\(1979\)009<0189:MOHSW>2.0.CO;2](http://dx.doi.org/10.1175/1520-0485(1979)009<0189:MOHSW>2.0.CO;2).
- Gerringa, L.J.A., Alderkamp, A.-C., Laan, P., Thuróczy, C.-E., De Baar, H.J.W., Mills, M.M., van Dijken, G.L., Van Haren, H., Arrigo, K.R., 2012. Iron from melting glaciers fuels the phytoplankton blooms in Amundsen Sea (Southern Ocean): Iron biogeochemistry. *Deep Sea Res. Part II Top. Stud. Oceanogr.* 71–76, 16–31. <http://dx.doi.org/10.1016/j.dsr2.2012.03.007>.
- Glenn, S., Jones, C., Twardowski, M., Bowers, L., Kerfoot, J., Kohut, J., Webb, D., Schofield, O., 2008. Glider observations of sediment resuspension in a Middle Atlantic Bight fall transition storm. *Limnol. Oceanogr.* 53 (5 part 2), 2180–2196. http://dx.doi.org/10.4319/lo.2008.53.5_part_2.2180.
- Glenn, S., et al., 2011. The trans-atlantic slocum glider expeditions: a catalyst for undergraduate participation in ocean science and technology. *Mar. Technol. Soc. J.* 45 (1), 52–67.
- Glenn, S.M., Grant, W.D., 1987. A suspended sediment stratification correction for combined wave and current flows. *J. Geophys. Res.* 92 (C8), 8244. <http://dx.doi.org/10.1029/JC092iC08p08244>.
- Grant, W.D., Madsen, O.S., 1986. The continental-shelf bottom boundary layer. *Annu. Rev. Fluid Mech.* 18 (1), 265–305. <http://dx.doi.org/10.1146/annurev.fl.18.010186.001405>.
- Ha, H.K., Wählin, A.K., Kim, T.W., Lee, S.H., Lee, J.H., Lee, H.J., Hong, C.S., Arneborg, L., Björk, G., Kalén, O., 2014. Circulation and Modification of warm deep water on the Central Amundsen Shelf. *J. Phys. Oceanogr.* 44 (5), 1493–1501. <http://dx.doi.org/10.1175/JPO-D-13-0240.1>.
- Hellmer, H., Jacobs, S., Jenkins, A., 1998. Ocean, Ice, and Atmosphere: Interactions at the Antarctic Continental Margin, Antarctic Research Series. In: Jacobs, S.S., Weiss, R.F. (Eds.), *Ocean, Ice, and Atmosphere: Interactions at the Antarctic Continental Margin*, Antarctic Research Series. American Geophysical Union, Washington, D. C.
- Jacobs, S., Giulivi, C., Dutrieux, P., Rignot, E., Nitsche, F., Mouginot, J., 2013. Getz Ice Shelf melting response to changes in ocean forcing. *J. Geophys. Res. Ocean.* 118, 4152–4168. <http://dx.doi.org/10.1002/jgrc.20298>.
- Jacobs, S.S., Hellmer, H.H., Jenkins, A., 1996. Antarctic Ice Sheet melting in the southeast Pacific. *Geophys. Res. Lett.* 23 (9), 957. <http://dx.doi.org/10.1029/96GL00723>.
- Jacobs, S.S., Jenkins, A., Giulivi, C.F., Dutrieux, P., 2011. Stronger ocean circulation and increased melting under Pine Island Glacier ice shelf. *Nat. Geosci.* 4 (8), 519–523. <http://dx.doi.org/10.1038/ngeo1188>.
- Jenkins, A., 1999. The impact of melting ice on ocean waters. *J. Phys. Oceanogr.* (3), 2370–2381.
- Jenkins, A., Jacobs, S., 2008. Circulation and melting beneath George VI Ice Shelf, Antarctica. *J. Geophys. Res.* 113 (C4), C04013. <http://dx.doi.org/10.1029/2007JC004449>.
- Jenkins, A., Dutrieux, P., Jacobs, S.S., McPhail, S.D., Perrett, J.R., Webb, A.T., White, D., 2010. Observations beneath Pine Island Glacier in West Antarctica and implications for its retreat. *Nat. Geosci.* 3 (7), 468–472. <http://dx.doi.org/10.1038/ngeo890>.
- Joughin, I., Smith, B.E., Medley, B., 2014a. Marine ice sheet collapse potentially underway for the Thwaites Glacier Basin, West Antarctica. *Science* 344 (6185), 735–738. <http://dx.doi.org/10.1126/science.1249055>.
- Joughin, I., Smith, B.E., Medley, B., 2014b. Marine ice sheet collapse potentially underway for the Thwaites Glacier Basin, West Antarctica. *Science* (80), 1. <http://dx.doi.org/10.1038/ngeo1188>.
- Kahl, L.A., Schofield, O., Fraser, W.R., 2010. Autonomous gliders reveal features of the water column associated with foraging by adelic penguins. *Integr. Comp. Biol.* 50 (6), 1041–1050. <http://dx.doi.org/10.1093/icb/icq098>.
- Kohut, J., Bernard, K., Fraser, W., Oliver, M.J., Statscewich, H., Winsor, P., Miles, T., 2015. Studying the impacts of local oceanographic processes on Adélie Penguin foraging ecology. *Mar. Technol. Soc. J.* 48 (5), 25–34. <http://dx.doi.org/10.4031/MTSJ.48.5.10>.
- Kohut, J.T., Haldeman, C., Kerfoot, J., 2014. Monitoring dissolved oxygen in New Jersey Coastal waters using autonomous gliders., Washington, D.C.
- Lee, S.H., Kim, B.K., Yun, M.S., Joo, H., Yang, E.J., Kim, Y.N., Shin, H.C., Lee, S., 2012. Spatial distribution of phytoplankton productivity in the Amundsen Sea, Antarctica. *Polar Biol.* 35 (11), 1721–1733. <http://dx.doi.org/10.1007/s00300-012-1220-5>.
- Madsen, O.S., Wright, L.D., Boon, J.D., Chisholm, T.A., 1993. Wind stress, bed roughness and sediment suspension on the inner shelf during an extreme storm event. *Cont. Shelf Res.* 13, 1303–1324. [http://dx.doi.org/10.1016/0278-4343\(93\)90054-2](http://dx.doi.org/10.1016/0278-4343(93)90054-2).
- McDougall, T., 1990. Bulk properties of “hot smoker” plumes. *Earth Planet. Sci. Lett.* 99, 185–194.
- McLean, S., 1991. Depth-integrated suspended-load calculations. *J. Hydraul. Eng.* 117 (11), 1440–1458.
- Miles, T., Glenn, S., Schofield, O., 2013. Temporal and spatial variability in fall storm induced sediment resuspension on the mid-Atlantic bight. *Cont. Shelf Res.* 63.
- Mouginot, J., Rignot, E., Scheuchl, B., 2014. Sustained increase in ice discharge from the Amundsen Sea Embayment, West Antarctica, from 1973 to 2013. *Geophys. Res. Lett.* 41, 1576–1584. <http://dx.doi.org/10.1002/2013GL059069>.
- Mrvaljevic, R.K., et al., 2013. Observations of the cold wake of Typhoon Fanapi (2010). *Geophys. Res. Lett.* 40 (2), 316–321. <http://dx.doi.org/10.1029/2012GL054282>.
- Padman, L., Fricker, H.A., Coleman, R., Howard, S., Erofeeva, L., 2002. A new tide model for the Antarctic ice shelves and seas. *Ann. Glaciol.* 34 (1), 247–254.

- Pelland, N.A., Eriksen, C.C., Lee, C.M., 2013. Subthermocline eddies over the Washington Continental Slope as observed by seagliders, 2003–09. *J. Phys. Oceanogr.* 43 (10), 2025–2053. <http://dx.doi.org/10.1175/JPO-D-12-086.1>.
- Planquette, H., Sherrell, R.M., Stammerjohn, S., Field, M.P., 2013. Particulate iron delivery to the water column of the Amundsen Sea, Antarctica. *Mar. Chem.* 153, 15–30. <http://dx.doi.org/10.1016/j.marchem.2013.04.006>.
- Pritchard, H.D., Ligtenberg, S.R.M., Fricker, H.A., Vaughan, D.G., van den Broeke, M. R., Padman, L., 2012. Antarctic ice-sheet loss driven by basal melting of ice shelves. *Nature* 484 (7395), 502–505. <http://dx.doi.org/10.1038/nature10968>.
- Randall-Goodwin, E., 2012. Detecting meltwater in the Amundsen Sea Polynya region, west Antarctica, University of California Santa Cruz.
- Randall-Goodwin, E., et al., 2015. Freshwater distributions and water mass structure in the Amundsen Sea Polynya region, Antarctica. *Elem. Sci. Anthr.* 3:000065. <http://dx.doi.org/10.12952/journal.elementa.000065>.
- Rignot, E., Jacobs, S.S., 2002. Rapid bottom melting widespread near Antarctic Ice Sheet grounding lines. *Science* 296 (5575), 2020–2023. <http://dx.doi.org/10.1126/science.1070942>.
- Rignot, E., Bamber, J.L., van den Broeke, M.R., Davis, C., Li, Y., van de Berg, W.J., van Meijgaard, E., 2008. Recent Antarctic ice mass loss from radar interferometry and regional climate modelling. *Nat. Geosci.* 1 (2), 106–110. <http://dx.doi.org/10.1038/ngeo102>.
- Rignot, E., Jacobs, S., Mougintot, J., Scheuchl, B., 2013. Ice-shelf melting around Antarctica. *Science* 341 (6143), 266–270. <http://dx.doi.org/10.1126/science.1235798> (80-).
- Rignot, E., Mougintot, J., Morlighem, M., Seroussi, H., Scheuchl, B., 2014. Widespread, rapid grounding line retreat of Pine Island, Thwaites, Smith, and Kohler glaciers, West Antarctica, 3502–3509. <http://dx.doi.org/10.1002/2014GL061040>. Received.
- Schmidtke, S., Heywood, K.J., Thompson, A.F., Aoki, S., 2014. Multidecadal warming of Antarctic waters. *Science* 346 (6214), 1227–1231. <http://dx.doi.org/10.1126/science.1256117>.
- Schofield, O., et al., 2007. Slocum Gliders: Robust and ready. *J. F. Robot.* 24 (6), 473–485. <http://dx.doi.org/10.1002/rob.20200>.
- Schofield, O., et al., 2013. Penguin biogeography along the west Antarctic peninsula: testing the canyon hypothesis with Palmer LTER Observations. *Oceanography* 26 (3), 204–206. <http://dx.doi.org/10.5670/oceanog.2013.63>.
- Schofield, O.M., Miles, T.N., Alderkamp, A.-C., Lee, S., Haskins, C., Rogalsky, E., Sipler, Sherrell, R.M., Yager, P.L., 2015. In Situ phytoplankton distributions in the Amundsen Sea polynya measured by autonomous gliders, *Elem. Sci. Anthr.*, 3, 2015 (in press).
- Smith, J. a, Hillenbrand, C.-D., Kuhn, G., Klages, J.P., Graham, A.G.C., Larter, R.D., Ehrmann, W., Moreton, S.G., Wiers, S., Frederichs, T., 2014. New constraints on the timing of West Antarctic ice sheet retreat in the eastern Amundsen Sea since the Last Glacial Maximum. *Glob. Planet. Change* 122, 224–237. <http://dx.doi.org/10.1016/j.gloplacha.2014.07.015>.
- Smith, W.O., Comiso, J.C., 2008. Influence of sea ice on primary production in the Southern Ocean: a satellite perspective. *J. Geophys. Res.* 113, 1–19. <http://dx.doi.org/10.1029/2007JC004251>.
- Stammerjohn, S., Massom, R., Rind, D., Martinson, D., 2012. Regions of rapid sea ice change: an inter-hemispheric seasonal comparison. *Geophys. Res. Lett.* 39 (6). <http://dx.doi.org/10.1029/2012GL050874>, n/a–n/a.
- Sunda, W.G., Huntsman, S.A., 1997. Interrelated influence of iron, light and cell size on marine phytoplankton growth. *Nature* 390 (1977), 389–392. <http://dx.doi.org/10.1038/37093>.
- Sutterley, T.C., Velicogna, I., Rignot, E., Mougintot, J., Flament, T., van den Broeke, M. R., van Wessem, J.M., Reijmer, C.H., 2014. Mass loss of the Amundsen Sea embayment of west Antarctica from four independent techniques. *Geophys. Res. Lett.* . <http://dx.doi.org/10.1002/2014GL061940>
- Thoma, M., Jenkins, A., Holland, D., Jacobs, S., 2008. Modelling Circumpolar Deep Water intrusions on the Amundsen Sea continental shelf, Antarctica. *Geophys. Res. Lett.* 35 (18), L18602. <http://dx.doi.org/10.1029/2008GL034939>.
- Thompson, A.F., Heywood, K.J., Schmidtke, S., Stewart, A.L., 2014. Eddy transport as a key component of the Antarctic overturning circulation. *Nat. Geosci.* 7. <http://dx.doi.org/10.1038/ngeo2289>.
- Thurnherr, A.M., 2010. A practical assessment of the errors associated with full-depth LADCP profiles obtained using teledyne RDI workhorse acoustic doppler current profilers. *J. Atmos. Ocean. Technol.* 27, 1215–1227. <http://dx.doi.org/10.1175/2010TECH0708.1>.
- Todd, R.E., Rudnick, D.L., Mazloff, M.R., Davis, R.E., Cornuelle, B.D., 2011. Poleward flows in the southern California current system: glider observations and numerical simulation. *J. Geophys. Res.* 116 (C2), C02026. <http://dx.doi.org/10.1029/2010JC006536>.
- Wählin, A.K., Yuan, X., Björk, G., Nohr, C., 2010. Inflow of warm Circumpolar Deep Water in the Central Amundsen Shelf. *J. Phys. Oceanogr.* 40 (6), 1427–1434. <http://dx.doi.org/10.1175/2010JPO4431.1>.
- Wählin, A.K., Kalén, O., Arneborg, L., Björk, G., Carvajal, G.K., Ha, H.K., Kim, T.W., Lee, S.H., Lee, J.H., Stranne, C., 2013. Variability of warm deep water inflow in a submarine trough on the Amundsen Sea shelf. *J. Phys. Oceanogr.* 43 (10), 2054–2070. <http://dx.doi.org/10.1175/JPO-D-12-0157.1>.
- Wählin, A.K., Muench, R.D., Arneborg, L., Björk, G., Ha, H.K., Lee, S.H., Alsén, H., 2012. Some implications of ekman layer dynamics for cross-shelf exchange in the Amundsen Sea. *J. Phys. Oceanogr.* 42 (9), 1461–1474. <http://dx.doi.org/10.1175/JPO-D-11-041.1>.
- Wählin, A.K., Kalén, O., Assmann, K.M., Darelius, H.K., Ha, Lee, S.H., 2015. Sub-inertial oscillations on the central Amundsen Shelf. *J. Phys. Oceanogr.* (in press)
- Walker, D.P., Brandon, M.A., Jenkins, A., Allen, J.T., Dowdeswell, J.A., Evans, J., 2007. Oceanic heat transport onto the Amundsen Sea shelf through a submarine glacial trough. *Geophys. Res. Lett.* 34 (2), L02602. <http://dx.doi.org/10.1029/2006GL028154>.
- Walker, D.P., Jenkins, A., Assmann, K.M., Shoosmith, D.R., Brandon, M.A., 2013. Oceanographic observations at the shelf break of the Amundsen Sea, Antarctica. *J. Geophys. Res. Ocean.* 118, 2906–2918. <http://dx.doi.org/10.1002/jgrc.20212>.
- Webb, D.C., Simonetti, P.J., Jones, C.P., 2001. SLOCUM: an underwater glider propelled by environmental energy. *IEEE J. Ocean. Eng.* 26 (4), 447–452. <http://dx.doi.org/10.1109/48.972077>.
- Yager, P.L., Sherrell, L.M., Stammerjohn, S.E., Alderkamp, A.-C., Schofield, O., Abrahamson, E.P., Arrigo, K.R., Bertilsson, S., Garay, D., Guerrero, R., 2012. ASPIRE: the Amundsen Sea Polynya international research expedition. *Oceanography* 25 (3), 40–53.